Bachelorthesis
Colloids in Low-polar Solvent under Influence of an Electric Field

Jasper Clarijs
3507858
Utrecht University
Department of Physics and Astronomy

January 9, 2013

Colloids in Low-polar Solvent under Influence of an Electric Field
Bachelorthesis
Jasper Clarijs
3507858

Supervisors
Dr. Bing Liu
Dr. Arnout Imhof

Soft Condensed Matter
Debye institute
Department of Physics and Astronomy
Utrecht University

Abstract

In this thesis we discuss the behaviour of suspended bullet-shaped rods in electric fields. Confocal microscopy is used to observe rodlike silica particles under the influence of a 1 MHz alternating electric field. Particle tracking software allows us to obtain the angle between the rods and the direction of the electric field, from which we calculate the two dimensional nematic order parameter. The results are compared with a theoretical model assuming ellipsoidal particles in electric fields. This model agrees with our experimental results. For high enough electric fields, the rodlike particles align with the electric field. We also wish to know the zeta potential and charge on the rods. Since no theoretical model exists relating macroscopic properties to these quantities we use spherical silica particles as an approximation. We observe suspended spherical silica particles under influence of a non-alternating electric field at two different concentrations using confocal microscopy and obtain their speeds using particle tracking software. Their electrophoretic mobilities are calculated while considering the effects of gravity and flows of the solvent. From the mobilities the zeta potential and particle charge are calculated, resulting in between 40 to 521 unit charges per sphere and zeta potentials ranging from 11.2 mV to 145 mV.

Contents

1 Introduction

For many years now researchers have been experimenting with so called colloids, particles with sizes between nanometers and several micrometers. Since colloids undergo phase transitions like ordinary atoms and molecules while being visible under a microscope, they serve well as a means of study of phase behaviour [1]. The study of colloids has also led to numerous applications such as coatings, electronic ink and photonic crystals [2, 3, 4].

1.1 Colloids

Colloids are, as aforementioned, small particles which serve well as a model for phase behaviour. The main reason for this is the fact that colloids undergo Brownian motion, which causes them to move around in a random fashion due to thermal fluctuations of the surrounding solvent [5]. Some common examples of colloids are blood, milk, mayonnaise and paint. For this thesis colloidal rods and spheres and their behaviour in electric fields where examined.

1.2 Colloids in electric fields

The colloids we consider in this thesis are either rodlike or spherically shaped. When colloidal rods are placed in an electric field, and the rods' dielectric constant differs from the solvent's dielectric constant, the rods obtain an induced polarization [6]. Therefore they start to behave as small dipoles, and dipole-dipole interactions may change some of the rods' macroscopic properties, such as their orientation. Since the effects of electric fields are fully reversible, electric fields provide us with a very interesting way of manipulating our colloids. For this thesis we research the effect of 1 MHz alternating electric fields with different field strengths on the orientation of rodlike particles. We use a high frequency alternating field so that the rods' double layers do not get polarized. We would like to know the charge and zeta potential of the rods as well. Since no theoretical model exists relating macroscopic properties to these quantities we use spherical silica particles as an approximation. We research the effects of a steady electric field applied to spherical colloids, at different field strengths. Since the colloids are charged (due to the dissociation of a hydrogen from silica's outer hydroxylgroups), they move in or against the direction of the electric field. In the following sections, first we

discuss the theory of the behaviour of rodlike particles in an alternating electric field. Next we discuss our experimental and analytical methods and then we show the results concerning the rodlike particles. Secondly we discuss the theory of the behaviour of suspended spherical colloids in a steady electric field. Then we again look at the experimental and analytical methods and present the corresponding results. Finally we shortly consider all the results and give an outlook for these kind of experiments.

2 Theory: rodlike particles

2.1 The ellipsoid model

We wish to be able to predict the behaviour of rods in an electric field theoretically. For a comparison between theory and experiment, we have to find a model which resembles our particles well. Our rodlike particles are nearly spherocylinders: they look like bullets, as shown in fig. 2.1.

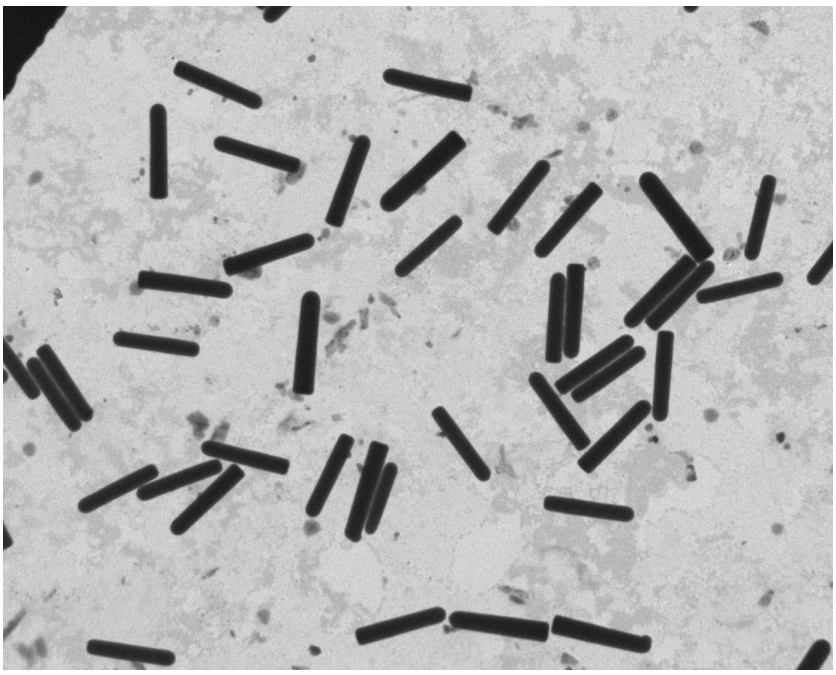

Figure 2.1: Image made with a Transmission Electron Microscope of the rodlike particles

It was shown in [7] by Venermo and Sihvola that the polarizability of circular cylinders differs little from the polarizability of ellipsoids. Venermo and Sihvola showed that for aspect ratios between 0 and 10 the difference in polarization between circular cylinders and ellipsoids was less than 10%. Therefore we compare our experiments with a model for ellipsoids for which we can analytically calculate the polarization [8]. The polarizability in the direction of the ith axis is given by

$$\alpha_i = \frac{\tau - 1}{1 + N_i(\tau - 1)} \tag{2.1}$$

where τ=ϵ_c/ϵ_s, the dielectric constant of the colloids relative to that of the solvent. N_i is the depolarization factor in the direction of the ith axis, and symmetry tells us that $N_y = N_z = (1 - N_x)/2$ if we choose our coordinate system with one base vector along the long axis of the ellipsoid (denoted by subscript x) and two others perpendicular to that vector (denoted by subscripts y and z). N_x is then given by

$$N_x = \frac{1-e^2}{2e^3}(\ln(\frac{1+e}{1-e}) - 2e) \tag{2.2}$$

where e is the eccentricity,

$$e = \sqrt{1 - \frac{a_y^2}{a_x^2}} \tag{2.3}$$

with a_y and a_x the lengths of the ellipsoids along their respective axes. Now that the polarizability is known we can calculate the polarization $\vec{p} = \alpha V \vec{E}$ and from this we obtain the energy [9]

$$U = -A\vec{p} \cdot \vec{E} = -AV\alpha_{\theta,\phi}\vec{E} \cdot \vec{E} = -AV\alpha_{\theta,\phi}|\vec{E}|^2 \tag{2.4}$$

Here V is the volume of a rod, $\vec{E}$ is the electric field and a factor A is included to account for effects such as mutual induction [8]. This factor which will be further determined in section 4.3 using experimental data. The polarizability is specifically denoted as $\alpha_{\theta,\phi}$, since in spherical coordinates the relevant polarizability depends on those two angles. However, since θ and ϕ are mutually independent we can consider the orientational distribution in the x,y-plane only, or equivalently only consider θ. α_θ can be computed using $N_\theta = N_x \cos(\theta) + N_y \sin(\theta)$, where θ indicates both the dependence of α_θ on θ and α_θ being the polarizability in the direction of the electric field.

2.2 The nematic order parameter

Now we have calculated all the important physical quantities we can determine some order parameter which is relevant to this system. Since at high fields the rods in the sample tend to transit to the nematic liquid crystal phase [10], we consider the two dimensional nematic order parameter P to quantify the order in our system. This quantity is defined as the average over the ensemble of the cosine of twice the angle with the nematic director [11],

$$P = \langle \cos(2\theta) \rangle \tag{2.5}$$

where the nematic director points just in the same direction as the electric field. Since our system is always in thermal equilibrium during the experiments, we can use the Boltzmann distribution to model our ensemble

$$\Psi(\theta) = \frac{e^{-\beta U(\theta)}}{\int_0^{\frac{\pi}{2}} e^{-\beta U(\theta)} \mathrm{d}\theta} \tag{2.6}$$

such that

$$P(E) = \int_0^{\frac{\pi}{2}} \cos(2\theta)\Psi(\theta)\,\mathrm{d}\theta \tag{2.7}$$

3 Methods: rodlike particles

3.1 Experimental setup

The setup of the experiment is as follows. First we prepare a sample of colloids in a solvent which is fit for putting under a microscope and has the possibility of carrying an electric field over the solvent. A more detailed description of how this is done can be found in section 3.1.1. After the sample is made we put it under the microscope while being able to apply an electric field. This electric field is generated by an HP 33120A generator. This generator is connected to an amplifier (Krohn-Hite model 7602 wideband amplifier), then to a homemade voltage doubler and finally to our sample, where the electric field is created. We measure the voltage over the sample with a Tektronix TDS 3012B oscilloscope. Note that for our theory we use the root-mean-square value of the voltage since the voltage oscillates. The connections are all being made with coax-cables. We apply an oscillating field of 1 MHz while varying the field strength from 0 $V/\mu m$ to 0.09 $V/\mu m$ in 9 steps (an increase of roughly $9 \cdot 10^{-3}$ $V/\mu m$ each time). The rods are observed and recorded with a Leica SP2 DMIRB confocal microscope, of which the details will be further discussed in section 3.1.2.

3.1.1 Preparing the samples

The samples are made by using two-sided gold- and chrome-coated VitroCom glass capillaries which are able to take in some rods dispersed in a solvent via capillary forces. The gold/chrome coating is done using a Cressington 208Hr sputter coater. The solvent used is cyclohexylchloride (CHCl) and is chosen because of its matching refractive index and low dielectric constant of 7.4. The rods used are made of silica and prepared by dr. Bing Liu. The details of his preparation method can be found in [12]. The rods are coated with FITC to make them fluorescent under the confocal microscope. Some of the properties of the rods are listed in table 3.1.

Length (μm) and polydispersity	3.3 (6.3%)
Diameter (μm) and polydispersity	0.59 (8.7%)
Aspect ratio	5.6
Dielectric constant	4.5

Table 3.1: Some properties of the silica rods

After the capillary is nearly full with the dispersion (leaving a meniscus only at one side, if any) we use UV-glue to seal the capillary shut onto a glass slide, preventing any solvent to evaporate during the experiments. The next step is to attach wires to the coating to be able to apply a field over the sample. Using silverpaint and more UV-glue, a thin thermocouple alloy wire is attached to the capillary. Whenever the UV-glue has to cure under a UV-lamp, the sample is protected by a piece of aluminum foil. The thin wires are connected to thicker wires and the entire sample is reinforced with plain tape. The result is shown schematically in figure 3.1

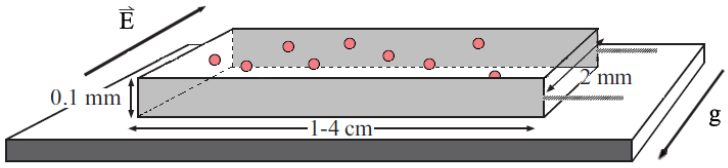

Figure 3.1: A glass slide, mounted by a glass capillary. This capillary is filled with rods suspended in solvent and coated with silverpaint. One wire is connected to the front side and one to the back side, as to establish an electric field. Note that the glue, thicker wires and tape are not shown for clarity

Finally it is checked if the two coated sides are isolated from eachother, since for an electric field there should be no current running through the sample.

3.1.2 Confocal microscopy

After preparing the sample we connect it to the generator and put it under the microscope. This technique is called confocal laser scanning microscopy (CLSM). A confocal microscope works by focussing light of a single point into a detector, and then scanning and adding many points to construct an image [9]. An overview is given in figure 3.3

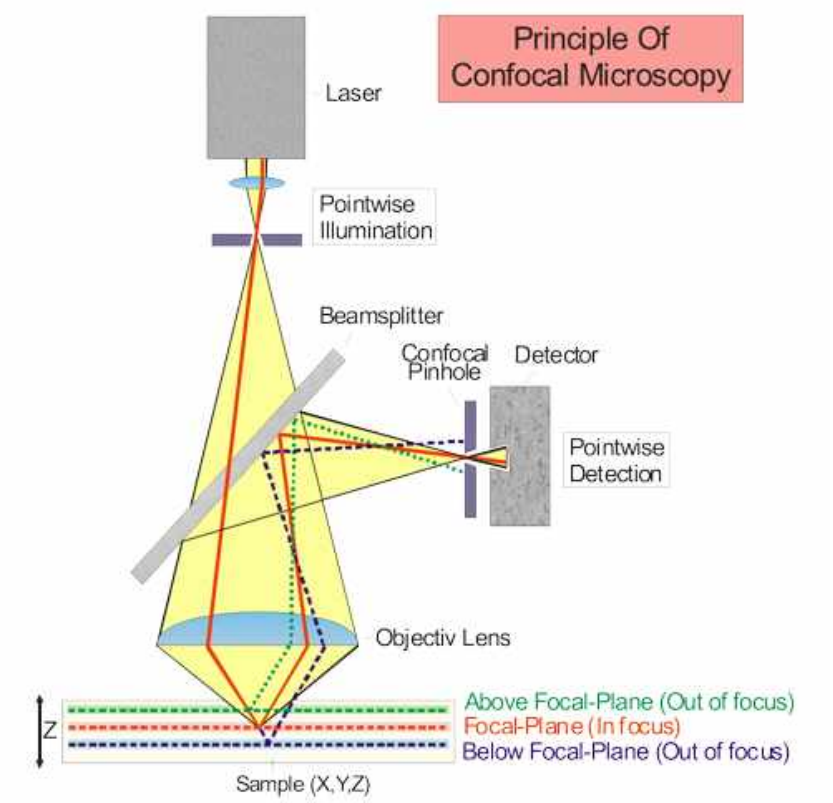

Figure 3.2: An overview of the functionality of a confocal microscope

A laser beam passes a convex lens and a pinhole. The resulting divergent bundle of light passes first a dichroic mirror and then the objective lens to illuminate the sample. The rods in the sample are fluorescently labeled and thus sent back light of a different colour, unable to pass back through the dichroic mirror. After being reflected the lightbeam passes a confocal pinhole such that only light from the focal point passed. Finally this light hits the detector, making up for one pixel of the total image. Scanning many points quickly makes up an entire image. In our case (observing the rodlike particles) we make images of 512 x 512 pixels in about 2.2 seconds.

3.2 Data analysis

After recording images of the sample with the confocal microscope, we use tracking software developed by Michiel Hermes to obtain information about

the particles. The tracking software is programmed to obtain the position (which was of no relevance for our goal) and the projection of particles on the x- and y-axis, with which we can determine the angle between the major axis of a rod and the electric field. Note that this angle is only an angle projected on the x,y-plane, since the images recorded with the microscope display projections of the rods. Using Wolfram Mathematica (version 8.0) the angles are calculated and further analysis of the data is done.

4 Results: Rodlike particles

4.1 Particle observation and tracking

To obtain enough angles for the averaging when calculating the two dimensional order parameter we take 100 images for every field strength at three different places, resulting in 300 images and at least 3000 angles for every field strength. To ensure the applied field is uniform all images were taken in the vertical middle of the capillary. All images are analysed by the software. In the following figures you can see one of the recorded images (left) and their tracked particles (right) for three different field strengths.

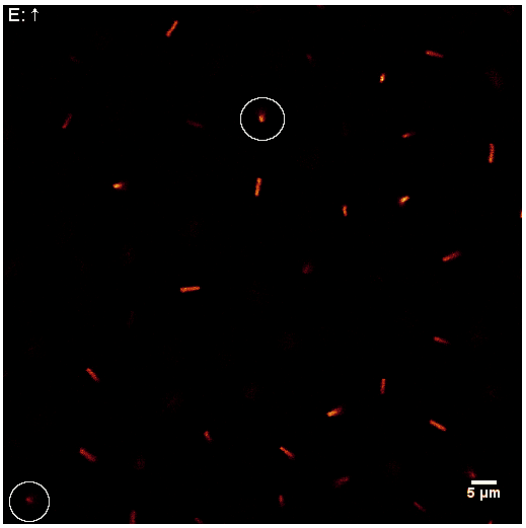

Figure 4.1: Rods (in red) in a field of 0 $V/\mu m$

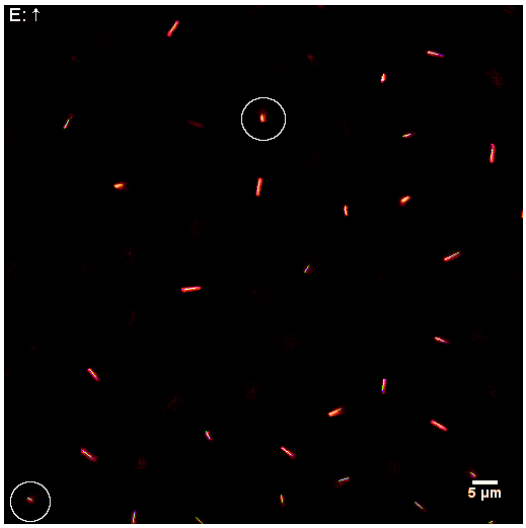

Figure 4.2: Rods (in red) and tracked rods (yellow lines) in a field of 0 $V/\mu m$

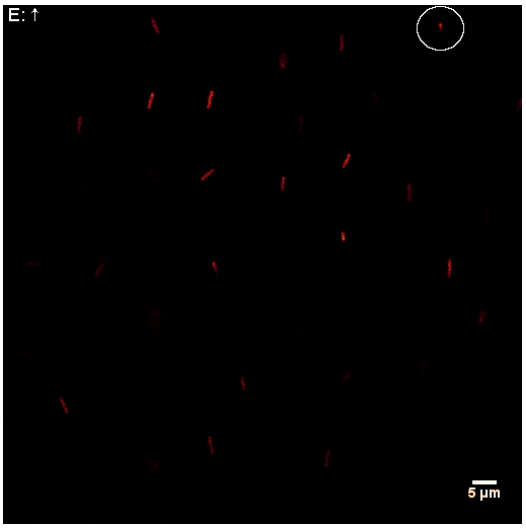

Figure 4.3: Rods (in red) in a field of 0.045 $V/\mu m$

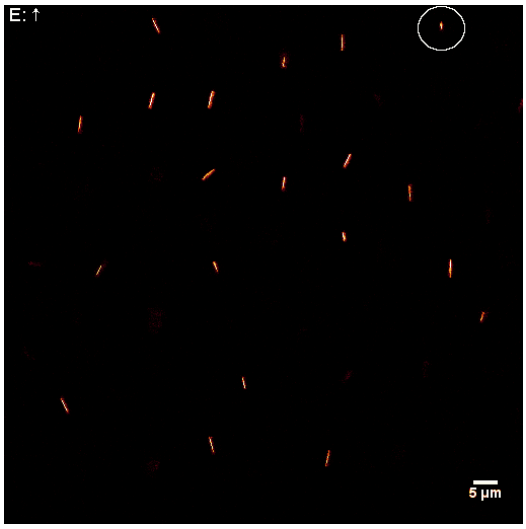

Figure 4.4: Rods (in red) and tracked rods (yellow lines) in a field of 0.045 $V/\mu m$

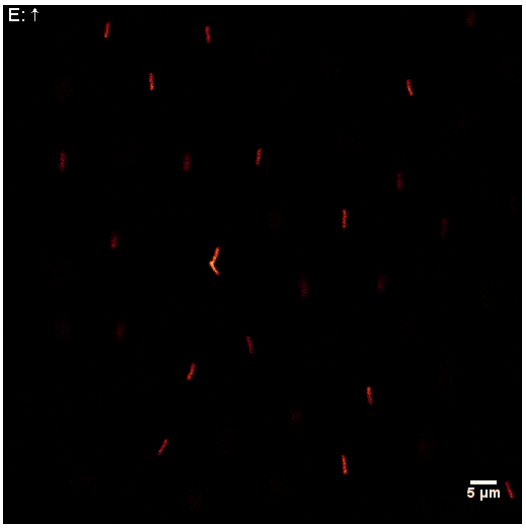

Figure 4.5: Rods (in red) in a field of 0.090 $V/\mu m$

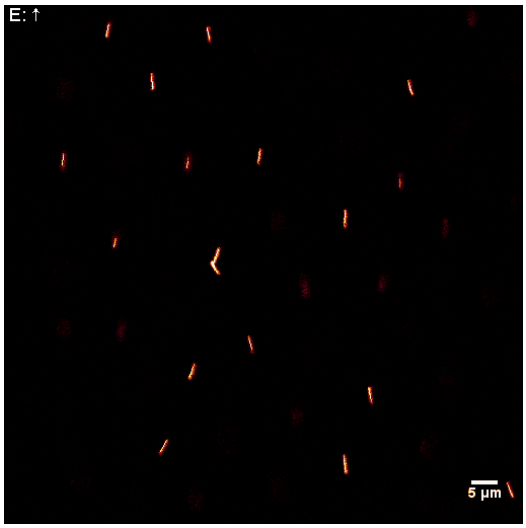

Figure 4.6: Rods (in red) and tracked rods (yellow lines) in a field of 0.090 $V/\mu m$

As can be seen in the images rods which are too blurry or not bright enough are not tracked by the software, as desired. Since we make two dimensional images of the sample, we only see the projection of the rods on our imaging plane. If a rod points upwards (or equivalently, downwards) we see that it's hard to obtain a proper two dimensional angle. Some of these rods are shown in the white circles in the figures above. Since these do not yield a proper angle, they are filtered out during the analysis. Only rods with a length of 80% of the actual length of a rod are kept after filtering. In figure 4.5 and figure 4.6 we can see a small aggregate of two rods in the middle of the pictures. Such aggregates were uncommon and their contribution to the angles can therefore be neglected.

4.2 Angle distribution

After extracting the data from the images with our tracking software, we are able to analyse the angles of the rods with the electric field. We find the following histograms, where on the vertical axis we have the number of counts and on the horizontal axis the angle θ. The width of each bin is $\pi/60$, resulting in 60 bins.

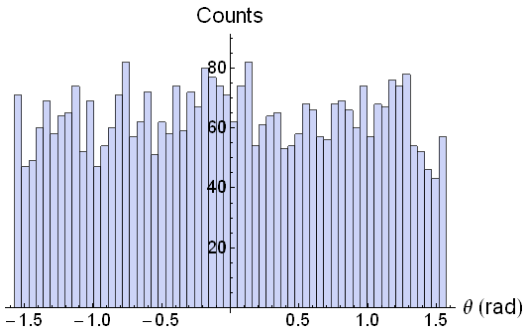

Figure 4.7: 3811 observed angles at a field strength of $E = 0V/\mu m$

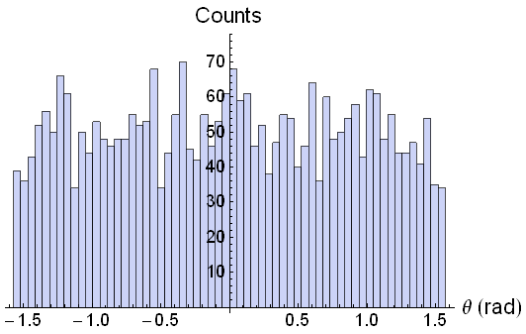

Figure 4.8: 3011 observed angles at a field strength of $E = 0.009V/\mu m$

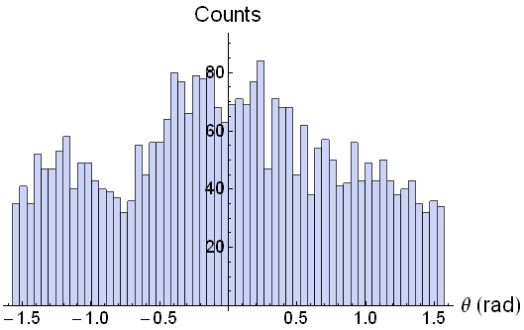

Figure 4.9: 3156 observed angles at a field strength of $E = 0.018V/\mu m$

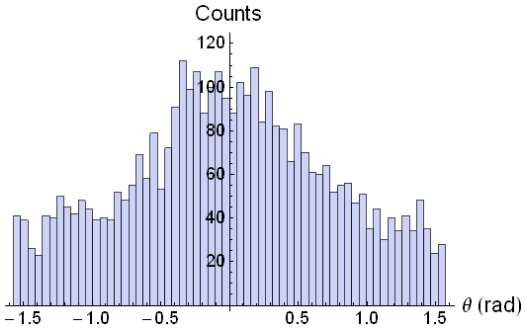

Figure 4.10: 3640 observed angles at a field strength of $E = 0.027V/\mu m$

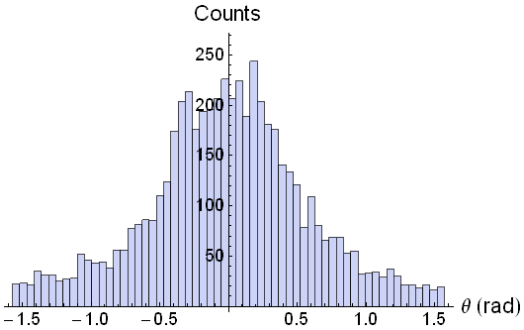

Figure 4.11: 5443 observed angles at a field strength of $E = 0.036V/\mu m$

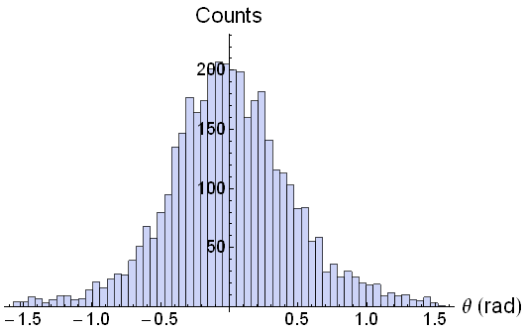

Figure 4.12: 3927 observed angles at a field strength of $E = 0.045V/\mu m$

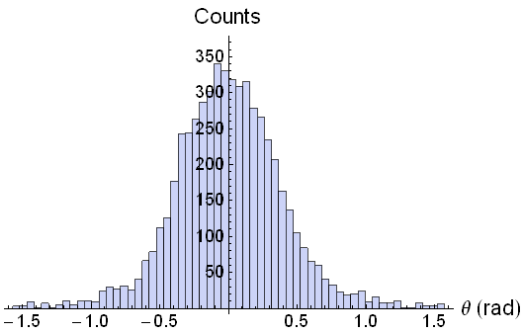

Figure 4.13: 5597 observed angles at a field strength of $E = 0.054V/\mu m$

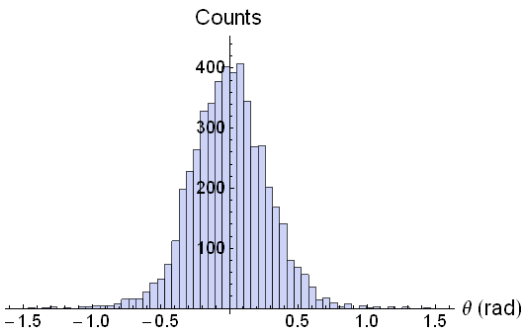

Figure 4.14: 5017 observed angles at a field strength of $E = 0.063V/\mu m$

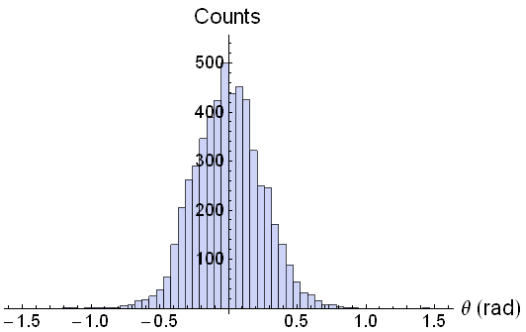

Figure 4.15: 5402 observed angles at a field strength of $E = 0.072V/\mu m$

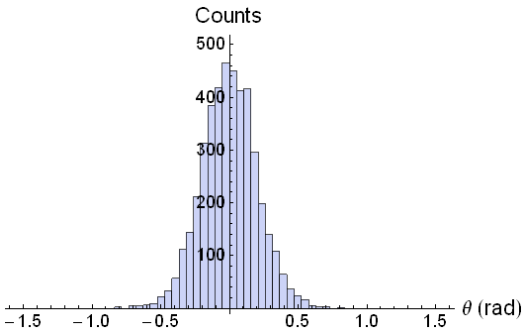

Figure 4.16: 4361 observed angles at a field strength of $E = 0.089V/\mu m$

We observe a reasonably flat histogram changing into a high-peaked one as the electric field strength increases, since the stronger the field, the stronger the induced polarizability will be, resulting in more alignment with the electric field. From all these observed angles we can directly calculate the nematic order parameter using the definition from eq. 2.5. The experimentally obtained values for the nematic order parameter for different values of the electric field strength are plotted in fig. 4.17.

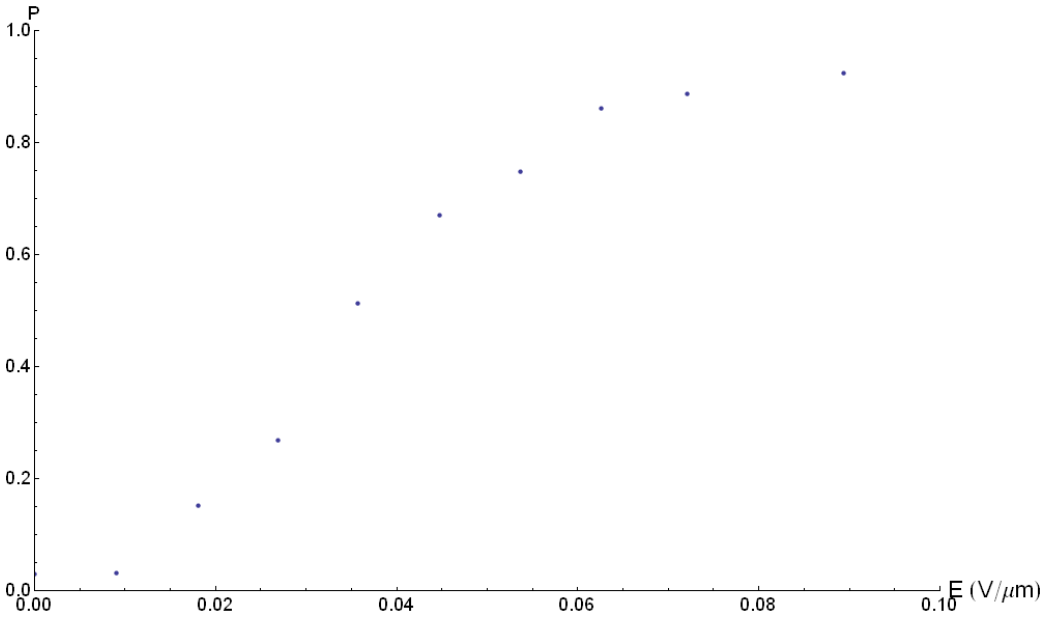

Figure 4.17: Experimentally found values for the nematic order parameter P against the electric field strength E

4.3 Determining the Boltzmann factor

Our next step is determining the Boltzmann factor in order to obtain a theoretical value for the nematic order parameter. But for the Boltzmann factor we need first to obtain a value for the factor A as mentioned in section 2.1. The way we do this is by viewing the relative occurrences of angles as statistical chances and fitting the Boltzmann factor of eq. 2.6 to that experimentally found data:

$$\Psi(\theta) = be^{\beta AV\alpha_{\theta,\phi}|\vec{E}|^2} \tag{4.1}$$

Where the factor b is just for normalisation. We fit the relative occurrences to $be^{a\alpha(\theta)}$ and find for every field strength the value of $a = \beta AV|\vec{E}|^2$. By plotting a against $|\vec{E}|^2$ we should find a linear relation of which the slope is the value of βAV. Once we have obtained that value we can further theoretically calculate the nematic order parameter as defined in eq. 2.7.

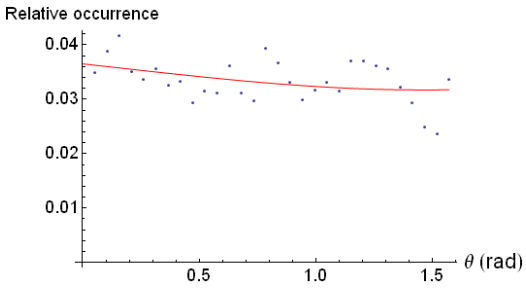

Figure 4.18: Relative occurrences of angles at a field strength of $E = 0V/\mu m$

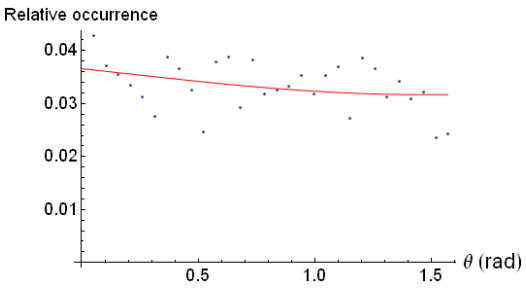

Figure 4.19: Relative occurrences of angles at a field strength of $E = 0.009V/\mu m$

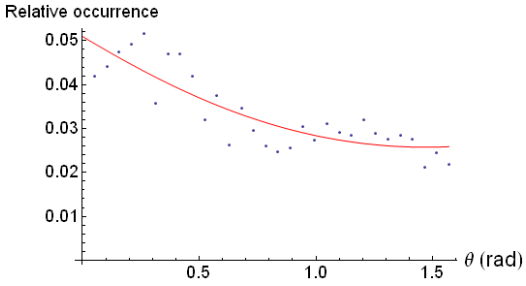

Figure 4.20: Relative occurrences of angles at a field strength of $E = 0.018V/\mu m$

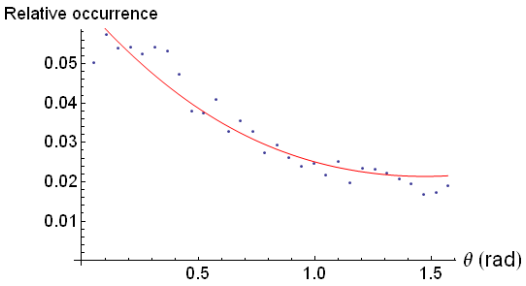

Figure 4.21: Relative occurrences of angles at a field strength of $E = 0.027V/\mu m$

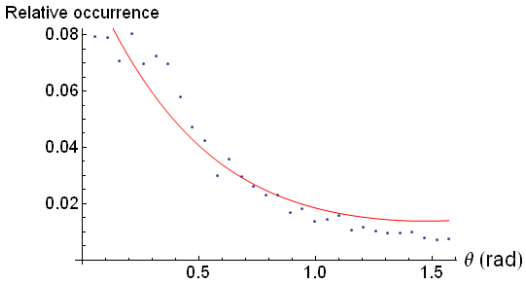

Figure 4.22: Relative occurrences of angles at a field strength of $E = 0.036V/\mu m$

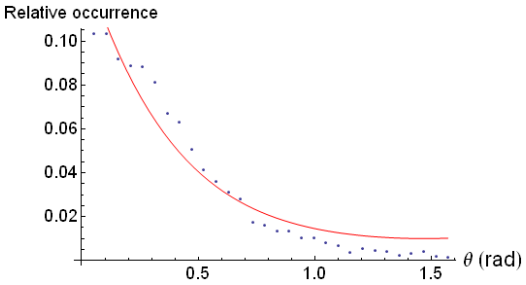

Figure 4.23: Relative occurrences of angles at a field strength of $E = 0.045V/\mu m$

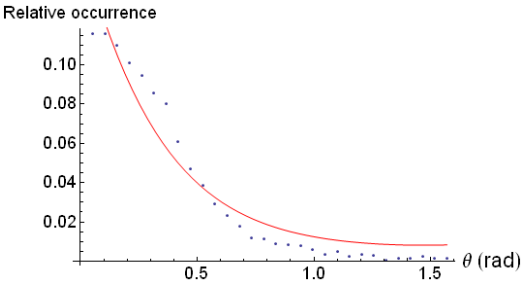

Figure 4.24: Relative occurrences of angles at a field strength of $E = 0.054V/\mu m$

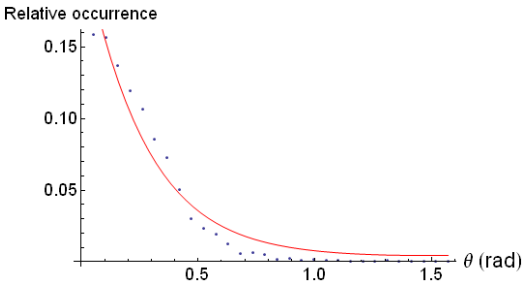

Figure 4.25: Relative occurrences of angles at a field strength of $E = 0.063V/\mu m$

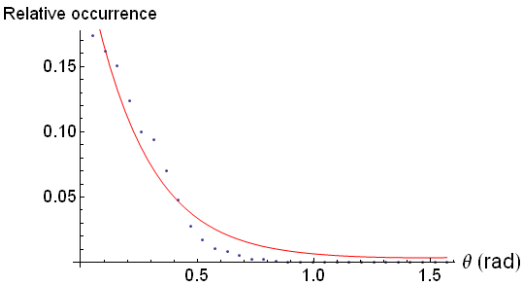

Figure 4.26: Relative occurrences of angles at a field strength of $E = 0.072V/\mu m$

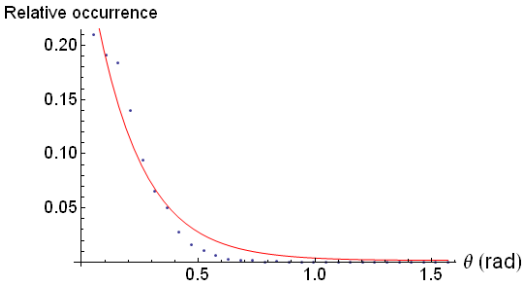

Figure 4.27: Relative occurrences of angles at a field strength of $E = 0.089V/\mu m$

In the figures 4.17 - 4.26, we have plotted the experimentally found relative occurrences of our rods (blue points) and fitted a function of the form of eq. 4.1 to it (red graph). Next, using the values of $|\vec{E}|^2$, we plot $\beta AV|\vec{E}|^2$ against $|\vec{E}|^2$. We also find a fit to the function $f(|\vec{E}|^2) = \beta AV|\vec{E}|^2$, such that the slope of this function gives us the value of βAV

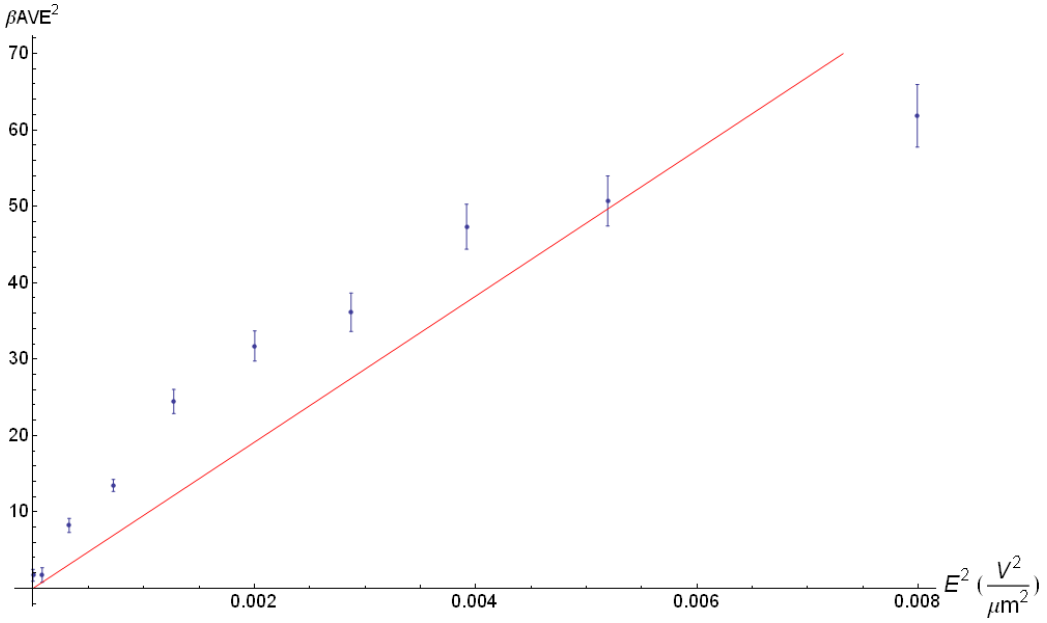

Figure 4.28: Experimentally found values for $\beta AV|\vec{E}|^2$ against $|\vec{E}|^2$ and their errorbars in blue, and a linear function fitting the points in red.

As can be seen in fig. 4.27, the straight line does not seem to fit our data very well. It seems as if for higher field strengths the slope lowers and our relation is no longer linear. To see if we have better linearity at low field strengths we also make a linear fit to only the first six points of our data. The result is shown in fig. 4.28

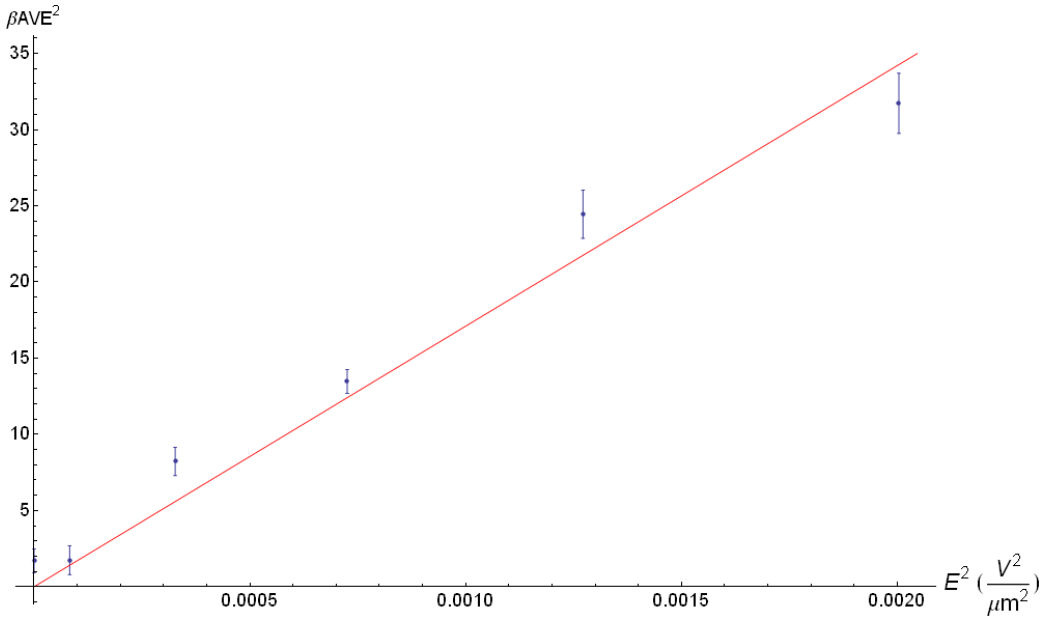

Figure 4.29: Experimentally found values for $\beta AV|\vec{E}|^2$ against $|\vec{E}|^2$ and their errorbars in blue, for only the first six points, and a linear function fitting these six points in red.

Now we see much more linearity in our data, indicating that higher order effects occur when our field strength is too high. We shall therefore use the value of βAV corresponding to fig. 4.28, namely $\beta AV = 1.71(\pm 0.9) \cdot 10^4 \mu m^2/V^2$.

4.4 The nematic order parameter

Now we finally have all the necessary parameters needed to calculate the nematic order parameter. We numerically calculate the integrals of eq. 2.6 and eq. 2.7 (using a stepsize of 10000) and show this plot together with the experimentally found values for the nematic order parameter, which we calculated directly from the angles using eq. 2.5.

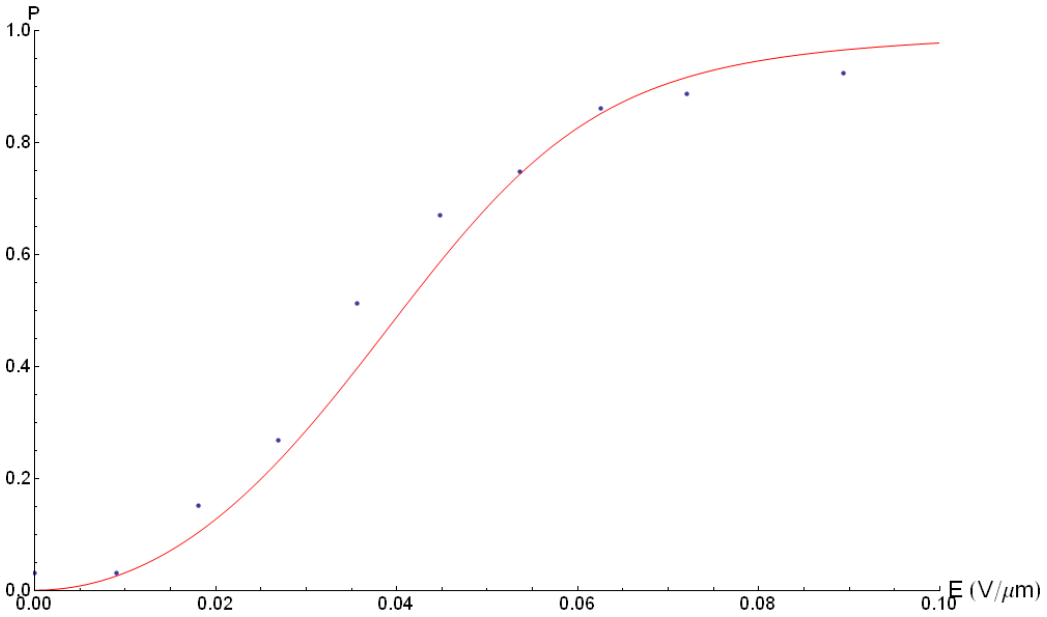

Figure 4.30: The nematic order parameter plotted against the electric field strength. Our experimentally found data is shown in blue points, our theoretically predicted curve is shown in red.

We see that the theoretical curve and experimental data agree reasonably. Note that the experimental values are too high at near-zero field strengths, and to low at high field strengths. This is because the nematic order parameter is defined to have a value between zero and one. Since any value is larger than zero, the average can never be zero at $\vec{E} = 0$ as theoretically predicted. Likewise, at high fields the average can never be one since any value of the nematic order parameter is less than one. However, the main reason the curves do not perfectly overlap (especially in the middle of the curve) is because of the use of our value for βAV, which is determined from only the first six field strengths.

Now that the nematic order parameter is known, we turn to spherical particles in a steady electric field in order to find their charge and zeta potential and approximate those quantities for our rodlike particles.

5 Theory: spherical particles

Since there is no theoretical model relating the charge and zeta-potential of rodlike particles to a macroscopic quantity, we need particles which resemble our silica rods well and for which a model does exist. We use silica spheres, particles with the same surface as the silica rods, and for which a model does exist. Here the electrophoretic mobility relates to the particle charge and the zeta potential. The electrophoretic mobility is defined in the following way [14]:

$$\vec{v}_E = \mu \vec{E} \tag{5.1}$$

So that the electrophoretic mobility μ is the ratio of the speed $|\vec{v}_E|$ a particle gains (due to the electric field) in the direction of the electric field to the electric field strength $|\vec{E}|$. When we measure the speed we do however not obtain the speed the particle has gained due to the electric field. Therefore we use Stokes' law [15] to find an expression for the mobility:

$$QE - \Delta mg = 6\pi\eta r v \tag{5.2}$$

where Q denotes the charge on a particle, E the electric field strength, Δm the difference between the mass moved by a particle and the mass of a particle itself, g the gravitational acceleration, η the dynamic viscosity of the solvent, r the radius of a particle and v its measured speed. We now consider this formula in the absence of gravity. Rearranging the terms we find an expression for the mobility:

$$\mu = \frac{v}{E} = \frac{Q}{6\pi\eta r} \tag{5.3}$$

If we now do consider gravity, we find

$$\frac{Q}{6\pi\eta r} - \frac{\Delta mg}{6\pi\eta r E} = \frac{v}{E} \tag{5.4}$$

so that, if we take $\frac{Q}{6\pi\eta r}$ to be our mobility,

$$\mu = \frac{v}{E} + \frac{\Delta mg}{6\pi\eta r E} \tag{5.5}$$

Conclusively we have to add a constant factor to the ratio of measured speed to electric field strength in order to account for gravity. The mobility is

related to the zeta potential via

$$\mu = \frac{2\epsilon_s \epsilon_0 \zeta}{3\eta} \tag{5.6}$$

where ϵ_s denotes the dielectric constant of the solvent, ϵ_0 the dielectric constant of the vacuum and ζ the zeta potential. We can calculate the electric force on a single particle using Stokes' law again:

$$Q = \frac{6\pi\eta r \vec{v}_{measured} + \Delta m g}{E} = 6\pi\eta r \mu \tag{5.7}$$

6 Methods: spherical particles

When measuring the electrophoretic mobility we apply the same method as we did for the rodlike particles: we use CLSM to observe our particles inside a capillary, and tracking software to locate our particles. To obtain their speeds, we link particles from frame to frame to form trajectories using IDL routines developed by John C. Crocker, David Grier and Erik Weeks [16].

6.1 Stationary layers

We observe particles at several heights, finding different speeds at different heights. This is due to motion of the fluid in which the particles are suspended. When applying an electric field to a closed capillary, counterions near the walls start to move along the wall, resulting in an electro-osmotic plug flow. Having to result in a net flow of zero in a closed capillary filled with an incompressible fluid, a counterflow ensues. This parabolic Poiseuille flow cancels the electro-osmotic plug flow exactly at the stationary layers, which for rectangular capillaries can be found at [17]

$$z_{stat} = h\sqrt{\frac{1}{3} + 4(\frac{2}{\pi})^5 \frac{h}{d}} \tag{6.1}$$

where z_{stat} denotes the distance from the center of the capillary, h is the height of the capillary and d the distance between the two walls furthest apart. Since the mobility at the stationary layers is unaffected by the flow of the solvent, we use this mobility to calculate the zeta potential and the particle charge.

6.2 Experimental setup

We use an experimental setup very similar to the one used for rodlike particles. We do change the capillaries we work with: instead of coated ones we put thin thermocouple alloy wires through ordinary capillaries to carry an electric field over the samples. A schematic overview can be found in figures 6.1 and 6.2.

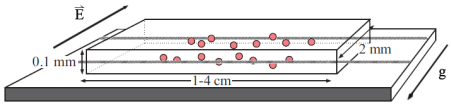

Figure 6.1: A glass slide, mounted by a glass capillary. This capillary is filled with spheres suspended in solvent and penetrated by two wires, which set up an electric field over the sample when they are connected to a power source. Note that as with the previously described sample, the glue, thicker wires and tape are not shown for clarity

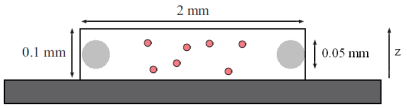

Figure 6.2: Cross-section of the sample. The grey circles inside the capillary represent the wires with a diameter of 0.05 mm

Note that we still glue the capillaries shut so that all that has changed is really the means of carrying a field over the sample. We use the same solvent as before (CHCl) in a sample, which has a dynamic viscosity of 1.5675 mPa s and a density of $0.998 \cdot 10^3 kg/m^3$. The stber silica spheres are monodisperse, have a radius of 0.7 μm and a density of $2.03 \cdot 10^3 kg/m^3$ [18]. After observing the spherical particles under the same microscope as the one we observed our rods with, we notice that too much sedimentation takes place in a short time, making it very hard to finish a dataset under the same circumstances. Therefore we set up the microscope so that it is laying on its side, so that the electric field is no longer perpendicular to gravity but rather aligns with it (albeit in opposite direction). This way we can counter the sedimentation. Our next step is to find a proper combination of field strength and volume fraction. A too high volume fraction or too high field strengths lead to string formation. A too low volume fraction still has quick sedimentation. A too low field strength will result in speeds in the direction of the field of comparable size to speeds due to Brownian motion, which will result in large deviations for the mobility. Therefore we do the experiment with two different samples called sample A and sample B. Sample A has a concentration of 0.5 volume-%, measuring it under influence of field strengths of 1.59 $mV/\mu m$ and 2.19 $mV/\mu m$. Sample B has a concentration of 0.25 volume-%, measuring it under influence of field strengths of 1.10 $mV/\mu m$, 1.59 $mV/\mu m$ and 0.66 $mV/\mu m$. We take recordings of the samples at several heights (up to twelve different heights) in order to establish a parabolic (z,μ)-curve due to the parabolic Poiseuille flow. Here μ denotes the electrophoretic mobility and z denotes the relative height, where the bottom is at z=0 and the top at z=1. Per recording we take 40 frames in order to minimize the time (as to delay the effects of sedimentation) but still have a large enough sample size.

7 Results: Spherical particles

7.1 Particle observation and tracking

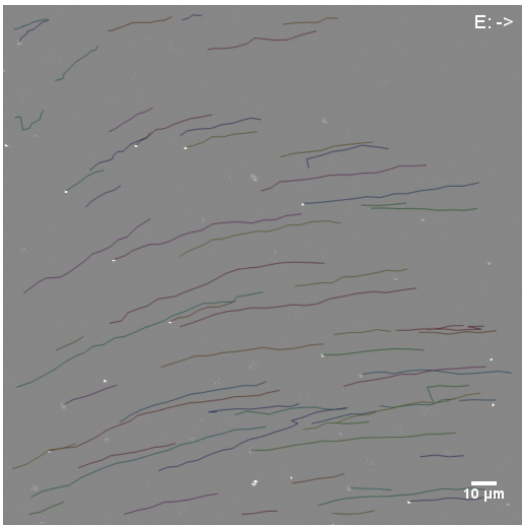

Figure 7.1: Observed particles (white spots) and their tracks found by the software (coloured lines) at t = 0 s. The direction of the field is to the right

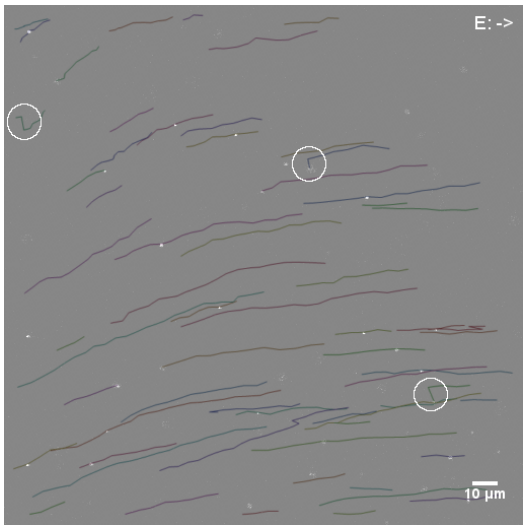

Figure 7.2: Observed particles (white spots) and their tracks found by the software (coloured lines) at t = 5 s. The direction of the field is to the right

In figures 4.1 and 4.2 we see the observed particles of sample B (the white spots) and the trajectories they follow according to our tracking software (the coloured lines). In fig. 4.2 we see most of the white spots have advanced along their trajectory, since this image is taken 10 ms later than fig. 4.1. Note that there are still many trajectories unoccupied by a particle. This is because particles move in and out of focus, so some trajectories will be occupied at a later time. We check the correctness of the tracking software by playing the video of the observed particles and see if they particles actually follow the trajectories. This is true for almost all trajectories, let alone a few exceptions. In fig. 4.2 we have encircled three of those exceptions. Here we see a sudden movement in the vertical direction, where a smoother motion in the direction of the field is expected. This is because of a tracking option which allows particles to disappear for two frames. If it resurfaces in an acceptable distance from where it disappeared in two frames or less, it is counted as the same particle. This causes the software to falsely recognize a different particle as the same, and linking their trajectories. Because these false trajectories

are uncommon, their contribution to the mean speed used for calculating the electrophoretic mobility can be ignored. Furthermore we see a slight tendency of moving upward of the particles as well, whereas the direction of the field is assumed to be purely from left to right. This may be caused by local deviations of the field, likely caused by the geometrical imperfections of our sample. Another cause of the tendency of moving upward may be a systematical error: when placing the sample in the microscope, it may not have been placed purely horizontal. Then gravity and the electric field would not be antiparallel. This effect will be ignored in processing our results since it does not occur for all recordings.

7.2 Mobility, zeta potential and charge

From the acquired data we calculate the mean speed of the particles. The speed is calculated by dividing the distance travelled by a particle in the direction of the electric field from one frame to another, by the time it took to get there; one second in our case. Using eq. 3.1 we calculate the mobility. This is done for several heights in the sample, so that we hope to establish a parabolic (z,μ)-curve due to the parabolic Poiseuille flow. The following curves are found.

7.2.1 Sample A

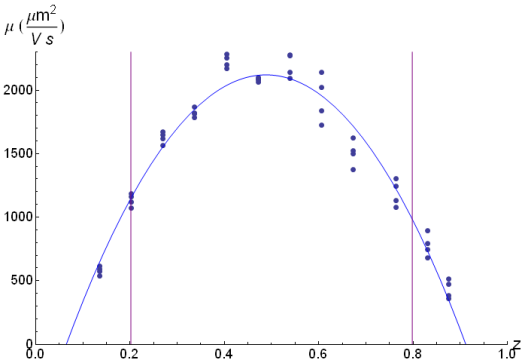

Figure 7.3: (z,μ)-diagram for sample A at $E = 1.59mV/\mu m$. The blue dots correspond to the experimental values of the mobility, the blue line is a parabola fitted to these points and the two purple lines represent the location of the stationary layers

Mobility μ ($\frac{\mu m^2}{Vs}$)	983.8 - 1149
Zeta potential ζ (mV)	35.3 - 41.2
Charges Z	127 - 148

Figure 7.4: Values for the mobility, zeta potential and number of unit charges of a silica sphere from batch A $E = 1.59mV/\mu m$. The two different values correspond to using the two different mobilities of the lower and the upper stationary layer

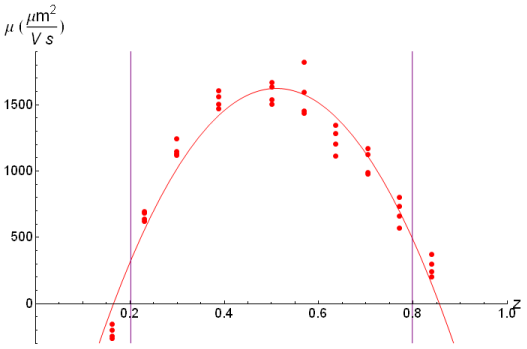

Figure 7.5: (z,μ)-diagram for sample A at $E = 2.19mV/\mu m$. The red dots correspond to the experimental values of the mobility, the red line is a parabola fitted to these points and the two purple lines represent the location of the stationary layers

Mobility μ ($\frac{\mu m^2}{Vs}$)	311.6 - 487.2
Zeta potential ζ (mV)	11.2 - 17.5
Charges Z	40 - 63

Figure 7.6: Values for the mobility, zeta potential and number of unit charges of a silica sphere from batch A at $E = 2.19mV/\mu m$. The two different values correspond to using the two different mobilities of the lower and the upper stationary layer

In the figures above we show the (z,μ)-diagrams and the resulting values for the mobility, zeta potential and number of unit charges. Note that we plot our experimentally found values of the mobility by calculating it per ten frames, resulting in four different mobilities at each height. By doing so we get an idea of the spread in the mobility. We see that the curves fit the data quite well most of the time. However, the resulting parabolas are usually quite asymmetrical, causing the values of the mobility to be different at both stationary layers. With these two values and equations 3.6 and 3.8 we calculate the zeta potential and the number of unit charges.

We observe a significant difference in mobilities at the two different field strengths. This indicates that the velocity is not linearly dependent on the electric field strength, so that $\mu = \mu(|\vec{E}|)$. We see that at both stationary layers, a higher field strength (red curve) seems to correlate to a lower mobility.

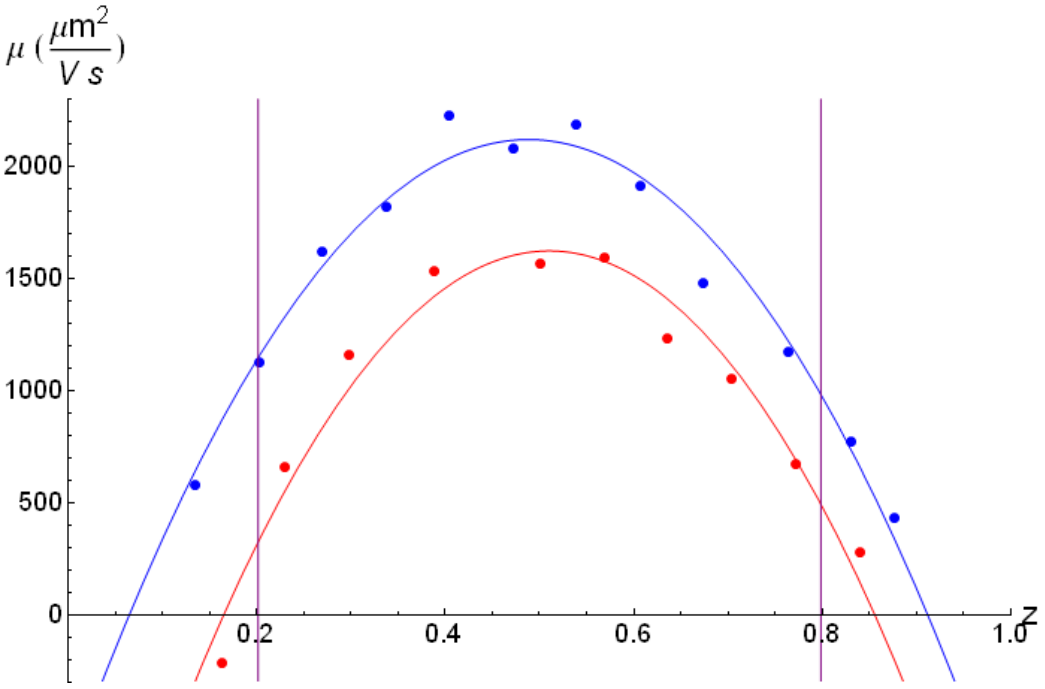

Figure 7.7: The (z, μ)-diagrams of sample A at $E = 1.59mV/\mu m$ and $E = 2.19mV/\mu m$ combined. Note that we average the mobility over the four points at each height

7.2.2 Sample B

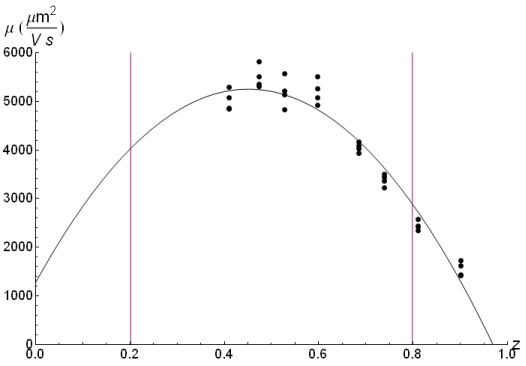

Figure 7.8: (z,μ)-diagram for sample B at $E = 0.66mV/\mu m$. The black dots correspond to the experimental values of the mobility, the black line is a parabola fitted to these points and the two purple lines represent the location of the stationary layers

Mobility μ ($\frac{\mu m^2}{Vs}$)	2890 - 4033
Zeta potential ζ (mV)	104 - 145
Charges Z	373 - 521

Figure 7.9: Values for the mobility, zeta potential and number of unit charges of a silica sphere from batch B at $E = 0.66mV/\mu m$. The two different values correspond to using the two different mobilities of the lower and the upper stationary layer

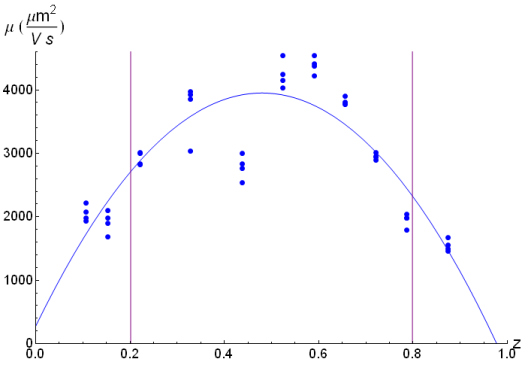

Figure 7.10: (z,μ)-diagram for sample B at $E = 1.10mV/\mu m$. The blue dots correspond to the experimental values of the mobility, the blue line is a parabola fitted to these points and the two purple lines represent the location of the stationary layers

Mobility μ ($\frac{\mu m^2}{Vs}$)	2329 - 2714
Zeta potential ζ (mV)	83.6 - 97.4
Charges Z	301 - 350

Figure 7.11: Values for the mobility, zeta potential and number of unit charges of a silica sphere from batch B at $E = 1.10mV/\mu m$. The two different values correspond to using the two different mobilities of the lower and the upper stationary layer

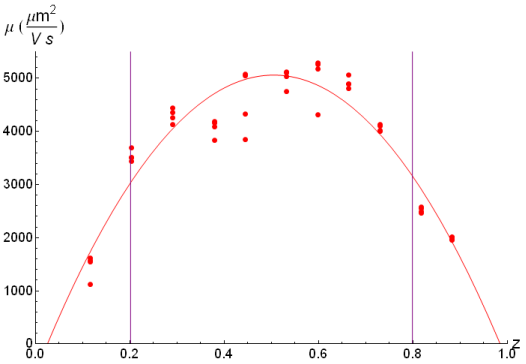

Figure 7.12: (z,μ)-diagram for sample B at $E = 1.59mV/\mu m$. The red dots correspond to the experimental values of the mobility, the red line is a parabola fitted to these points and the two purple lines represent the location of the stationary layers

Mobility μ ($\frac{\mu m^2}{Vs}$)	3039 - 3162
Zeta potential ζ (mV)	109 - 113
Charges Z	392 - 408

Figure 7.13: Values for the mobility, zeta potential and number of unit charges of a silica sphere from batch B at $E = 1.59mV/\mu m$. The two different values correspond to using the two different mobilities of the lower and the upper stationary layer

Here above too, we show the (z,μ)-diagrams and the resulting values for the mobility, zeta potential and number of unit charges. Also we show the spread in mobilities by taking the speed over 10 frames again. Once again we check the dependency of the mobility by putting the curves together in fig. 4.17.

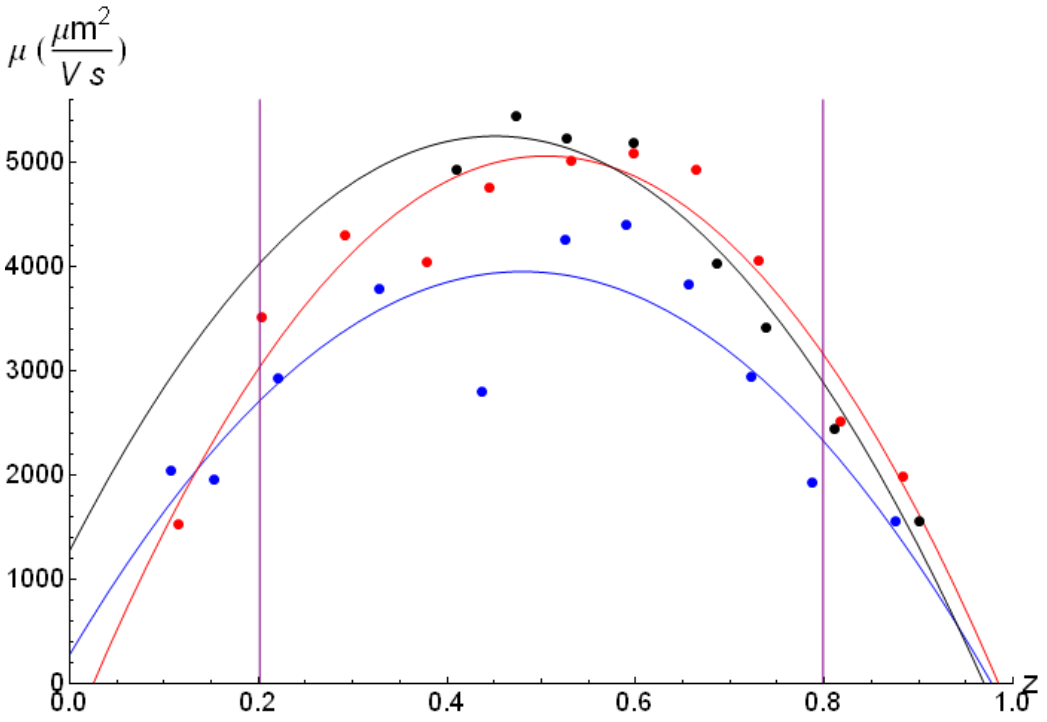

Figure 7.14: The (z, μ)-diagrams of sample B at $E = 0.66mV/\mu m$, $E = 1.10mV/\mu m$ and $E = 1.59mV/\mu m$ combined. Note that we average the mobility over the four points at each height

Once again we note that there are significant differences in the mobilities at the three different field strengths. However, this figure doesn't indicate whether the mobility increases or decreases with the field strength clearly as with sample A.

8 Conclusions

For the first part of this thesis we have observed rodlike silica particles in rapidly oscillating electric fields at different field strengths and considered the orientational order of the rods. The order was parameterised by the nematic order parameter and this parameter was also computed theoretically using a model concerning ellipsoids. We find that this model is capable of predicting the values of the nematic order parameter reasonably well. It shows a phase transition from an unordered dispersion to a liquid crystal. Nevertheless the model does not predict the dependency of the energy on the electric field strength well for higher field strengths. There doesn't seem to be linearity between the two for higher field strengths, indicating that the factor A as calculated in section 4.3 is field-dependent. Since we introduced the factor A to account for effects such as mutual induction contributing to the energy of a dipole, it is not strange to see this happen because the induction is caused by the electric field. Using a constant factor as in eq. 2.4 for the contribution to the energy of a dipole is thus not justified at all field strengths.

For the second part of this thesis we have observed spherical silica particles in a steady electric field, at different heights in the sample and at two different field strengths. Their speeds were measured and from it we calculated the mobility, the zeta potential and the number of unit charges on a sphere. The results are not unequivocal, since the mobilities at different stationary layers can differ by a factor of up to 1.56 (sample A, $E = 2.19 mV/\mu m$). The spread in mobilities result in a spread in zeta potential and charge on a sphere as well. This spread may be caused by the quick sedimentation of our samples due to density differences between silica and the solvent and the charge on the glass walls. These result in concentration differences at the stationary layers. Concentration differences affect the amount of hydrogen a colloid is able to dissociate to the solvent, so that the charge of a colloid and hence its mobility are affected as well.

9 Acknowledgements

Writing this thesis has proven to be hard work, and I could not have done it alone. Therefore I would like to express my gratitude to my supervisor, dr. Bing Liu, for answering all my questions, showing me the craft of experimenting (teaching me a lot during the process) and all the time he has put in helping me in general. It is much appreciated. I would also like to thank dr. Arnout Imhof for taking me into the soft condensed matter group and allowing to work on this thesis under his supervision. My final thanks go to my fellow students in the student room, all the PhD students and postdocs, and Peter Helferrich, helping me out countless times with lab supplies, computer practices and day-to-day business.

10 Bibliography

References

[1] W. Poon. Colloids as big atoms. *Science*, 304:830-831, 2004

[2] B. Comiskey, J.D. Albert, H. Yoshizawa and J. Jacobson. An electrophoretic ink for all-printed reflective electronic displays. *Nature*, 394:253, 1998

[3] E.D. Morrison. Synthesis of vanadium oxide colloidal dispersions for antistatic coating. *Mat. Res. Soc. Symp. Proc.*, 432:121-131, 1997

[4] Y. Vlasor, X. Bo, J. Sturm and D. Norris. On-chip natural assembly of silicon photonic bandgap crystals. *Nature*, 414:289, 2001

[5] M.D. Haw, COlloidal suspensions, Brownian motion, molecular reality: a short history. *J. Phys.: Cond. Mat.*, 19:7769, 2002

[6] H. Ma, W. Wen, W. Y. Tam and P. Sheng. Dielectric electrorheological fluids: theory and experiment. *Adv. Phys.*, 52"343, 2003

[7] J. Venermo and A. Sihvola. Dielectric polarizabaility of circular cylinder. *Journal of Electrostatics*, 63:101-117, 2005

[8] M. Mittal and E.M. Furst. Electric field-directed convective assembly of ellipsoidal colloidal particles to create optically and mechanically anisotropic thin films. *Advanced Functional Materials*, 19:3271-3278, 2009

[9] T.B. Jones, *Electromechanics of particles*, Cambridge University Press, New York City, NY 1995

[10] M. Rotunno, T. Bellinni, Y. Lansac and M.A. Glaser. Phase behavior of polarizable spherocylinders in external fields. *Journal of Chemical Physics*, 121:5541-5549, 2004

[11] D. Frenkel and R. Eppenga. Evidence for algebraic orientational order in a two-dimensional hard core nematic. *Physical Review A*, Volume 31, number 3, March 1985

[12] A. Kuijk, *Fluorescent colloidal silica rods - synthesis and phase behavior*, Thesis, Utrecht University, 2012

[13] V. Prassad, D. Semwogerere, E.R. Weeks, Confocal microscopy of colloids. *J. Phys.: Cond. Mat.*, 19, 113102, 2007

[14] F. Carrique, F.J. Arroyo and A.V. Delgado. Electrokinetics of concentrated suspensions of spherical colloidal particles with surface conductance, arbtirary zeta potential, and double-layer thickness in static electric fields. *J. Colloid Interface Sci.* 252:126-137, 2002

[15] STOKES LAW

[16] E. Weeks, (August 27, 2011). *Particle tracking using IDL*. Retrieved November 29, 2012, from http://www.physics.emory.edu/ weeks/idl/

[17] R. Hunter, *Zeta potential in colloid science*, Academic Press, London, 1981

[18] A. van Blaaderen and A. Vrij. Synthesis and Characterization of Colloidal Dispersions of Fluorescent, Monodisperse Silica Spheres. *Langmuir* 8:2921-2931, 1992